Climate Dynamics (2022) 59:1213–1232
https://doi.org/10.1007/s00382-022-06187-3

# The dynamical-statistical subseasonal prediction of precipitation over China based on the BCC new-generation coupled model

Jie Wu[1] · Hong-Li Ren[2] · Peiqun Zhang[1] · Yan Wang[3] · Ying Liu[1] · Chongbo Zhao[1] · Qiaoping Li[4]

Received: 23 September 2021 / Accepted: 28 January 2022 / Published online: 20 February 2022


**Abstract**
Skillful subseasonal prediction is crucial for meteorological disaster prevention and risk management. In this study, the subseasonal prediction skills of the new-generation coupled model of Beijing Climate Center (named as BCC-CSM2-HR) were evaluated, and a dynamical-statistical prediction model (DSPM) was developed to further improve pentad-mean precipitation predictions in China. The results show that although BCC-CSM2-HR can generally capture the climatological rain belt movement over eastern China, its skillful predictions for rainfall anomalies are basically confined within 3 pentads. By combining the dynamical model output and statistical method, a DSPM was built to capture the simultaneously coupled evolving patterns between anomalous precipitation and its atmospheric circulation predictors for each subregion of China, which was divided in terms of a cluster analysis. The 9-year independent validation shows that the prediction skills of DSPM had been significantly improved after 3 forecast pentads compared with the original model forecast. The skillful prediction can persist for a 6-pentad lead especially over the northern China and the Yangtze-Huaihe River Basin in the DSPM. As the major predictability sources of subseasonal forecasts, the Madden–Julian oscillation (MJO) and boreal summer intraseasonal oscillation (BSISO) are skillfully predicted by the BCC model for up to 23 days and 10–13 days, respectively. As a result, the improved performance of the DSPM can be largely attributed to its more realistic representation of MJO and BSISO associated circulation anomalies.

**Keywords** Subseasonal forecast · BCC S2S model · Dynamical-statistical prediction · Predictability sources · Madden–Julian oscillation (MJO)

## 1 Introduction

The subseasonal prediction (10–60 days) is subjected to the fast damping of atmospheric initial signals and the inadequate representation of boundary conditions. Therefore, the prediction skill of subseasonal prediction is relatively lower than weather forecasts (shorter than 10 days) and climate predictions (longer than 2 months), which has become the gap in seamless operational predictions (Brunet et al. 2010). However, subseasonal predictions for long-lasting extreme events (such as continuous rainstorms, heat waves and freezing snow) are particularly important for disaster prevention, risk management and agricultural planning (Zhang 2013).

Intraseasonal oscillation (ISO) is an important source of subseasonal predictability due to its relatively regular activity characteristics. In the tropics, intraseasonal variability is dominated by the Madden–Julian oscillation (MJO; Madden and Julian 1971, 1972), which is characterized by a planetary-scale eastward-propagating convection-circulation coupled pattern with time scales of 30–80 days (Zhang 2005; Adames and Wallace 2014; Li et al. 2020). By releasing abundant diabatic convective heating, the MJO will exert remarkable influences on global teleconnections (Stan et al. 2017), monsoon activity (Taraphdar et al. 2018a, b), tropical cyclone genesis (Zhao

✉ Hong-Li Ren
renhl@cma.gov.cn

1 CMA Climate Studies Key Laboratory and CMA-NJU Joint Laboratory for Climate Prediction Studies, National Climate Center, China Meteorological Administration, Beijing 100081, China

2 State Key Laboratory of Severe Weather, Chinese Academy of Meteorological Sciences, Beijing 100081, China

3 Shanxi Climate Center, Xi'an 710014, China

4 CMA Earth System Modeling and Prediction Centre (CEMC), China Meteorological Administration, Beijing 100081, China

et al. 2019), and extreme events (Ren and Ren 2017; Hsu et al. 2020). Other than the MJO, the intraseasonal variability in the Asian summer monsoon displays different features, such as northward or northwestward propagation with dual oscillation period peaks of 10–30 days and 30–60 days, which is recognized as the boreal summer intraseasonal oscillation (BSISO; Lee et al. 2013). Recent studies have revealed that the BSISO also plays an important role on the formation of extreme rainfall and heat waves over the eastern China by modulating anomalous water vapor transport and vertical circulation (Hsu et al. 2017; Ren et al. 2018). Therefore, the ISO is considered useful for bridging the gap between synoptic and climatic timescales. Additionally, recent studies have revealed that the quasi-biennial oscillation (QBO) (Zhang and Zhang 2018), snow cover (Li et al. 2018), stratosphere-troposphere interaction (Schwartz and Garfinkel 2020) and intraseasonal SST variability (Zhu et al. 2021) also act as additional potential predictability sources on subseasonal timescales.

Based on theoretical advances, several statistical models have been developed for subseasonal prediction, such as the linear regression pattern by the MJO, the "low-frequency weather map" and the principal oscillation pattern (Yang et al. 2012). Specifically, the spatial–temporal projection models (STPMs) proposed by Hsu et al. (2015) and Zhu et al. (2015) can capture the successively varying spatial and temporal information of coupled predictor-predictand patterns well, showing considerable skills for predicting summer rainfall, heat waves and cold winter days (Zhu and Li 2017, 2018). However, the statistical models that mainly rely on the significance of previous signals show limits in capturing intraseasonal variability at shorter forecast leads (e.g., 10–30 days) or predicting rapid swing events (Zhu and Li 2017).

Efforts have also been made to fill the prediction gap in the subseasonal time scale based on dynamical models (Vitart 2014; Kim et al. 2018), such as improving the initial conditions (Fu et al. 2011; Wu et al. 2020), optimizing ensemble strategies (Ham et al. 2012; Hudson et al. 2013; Green et al. 2017), refining air-sea coupling (Fu et al. 2013; Zhu et al. 2018) and developing more realistic physical processes (Hirons et al. 2013; Liu et al. 2019). In this context, the Subseasonal to Seasonal (S2S) prediction project (Vitart et al. 2017) provides an unprecedented opportunity to evaluate the latest subseasonal prediction ability of the 11 most advanced dynamical models in operational centers and research institutes worldwide. Recent studies have revealed that S2S models gain considerable skills in MJO (Lim et al. 2018), BSISO (Jie et al. 2017) and their associated convection predictions (Wang et al. 2019). However, the usefulness for direct precipitation predictions in dynamic model is generally limited to 2 weeks and mostly confined to the tropics (Andrade et al. 2019).

Several factors can contribute to the limited predictive skills of precipitation in dynamical models. For instance, S2S models still have difficulties in realistically representing extratropical responses to the MJO (Vitart et al. 2017) or capturing the ISO signals in extratropical and mid-latitude regions (Zheng et al. 2020). Therefore, potential benefits may be gained by effectively combining these dynamical models and empirical/statistical methods to calibrate precipitation predictions. Although previous studies on seasonal-scale prediction have shown the effectiveness of utilizing dynamical-statistical models (Liu et al. 2021a, b, c), few attempts have been made at the subseasonal timescale (Wu and Jin 2021).

As a participant in the S2S prediction project, the Beijing Climate Center-Climate System Model (BCC-CSM) has been widely used in operational subseasonal prediction and displays considerable skills for MJO and monsoon circulation prediction (Wu et al. 2016; Liu et al. 2017; Liu et al. 2021a, b, c). Compared with its previous version (BCC-CSM1.2), many improvements have been made for the latest model (BCC-CSM version 2-High Resolution, named as BCC-CSM2-HR) that participates in S2S project Phase II (Wu et al. 2021), such as a higher atmospheric resolution, implementation of a new data assimilation scheme (Liu et al. 2021a, b, c), and modification of convection and cloud physical processes (Wu et al. 2019). As a result, these improvements in BCC-CSM-HR contribute to better simulations performance than the previous version in many aspects (Wu et al. 2021). In this study, the latest BCC-CSM-HR model will be used to evaluate its ability to predict subseasonal precipitation anomalies and further develop a dynamical-statistical model to improve its prediction skill.

The remainder of this paper is organized as follows: The hindcast and observation data, as well as verification method, are introduced in Sect. 2. The subseasonal prediction performance of BCC-CSM-HR is evaluated in Sect. 3. The detailed procedure of the dynamical-statistical model and its advantages are given in Sect. 4. The possible predictability sources for the dynamic statistical model are examined in Sect. 5. A summary and discussion are presented in Sect. 6.

## 2 Model, data and method

### 2.1 Model hindcast data

The BCC new-generation dynamical prediction system based on BCC-CSM2-HR has participated in the S2S prediction project Phase II in place of BCC_CSM1.2. The atmospheric component of the BCC-CSM2-HR model has

an increased resolution, from T106L40 to T266L56, with the top layer and model lid at 0.156 and 0.092 hPa, respectively. Moreover, the dynamical core and model physics have also been updated, such as inclusion of spatially variant divergence damping processes and improved deep convection and cloud macrophysics schemes (Wu et al. 2019). The ocean and sea ice components are also updated from MOM4 and SIS4 to MOM5 and SIS5, respectively, with resolutions of 1/4° × 1/4° in the horizontal layer and 40 layers in depth. The land component is BCC-AVIM version 2 (Li et al. 2019). Following all of the above improvements, the model's representation of the ENSO seasonal cycle, the eastward propagation of the MJO, and the downward propagation of the QBO are much more reliable than the previous version (Wu et al. 2021).

Different from the fixed hindcast strategy used in the S2S project Phase I, the BCC-CSM2-HR adopted the on-the-fly hind strategy, and running twice a week (on Monday and Thursday) for a 60-day integration in the past 15 years. Each forecast consists of 4 ensemble members from a stochastic perturbation of physics tendencies (SPPT) scheme. The hindcast data used in this study were generated in 2020, which cover the period of 2005–2019. All the circulation variables were interpolated onto grids with a horizontal resolution of 2.5° × 2.5°, except for the precipitation data, which were interpolated onto a higher resolution (0.5° × 0.5°) grid in China.

## 2.2 Observational data

For model verification and dynamical-statistical model construction, the daily geopotential height, zonal wind, sea level pressure and specific moisture are taken from the National Centers for Environmental Prediction/National Center for Atmospheric Research (NCEP/NCAR) Reanalysis version 1 dataset (Kalnay et al. 1996), and the daily outgoing longwave radiation (OLR) data are from the National Oceanic and Atmospheric Administration (NOAA; Liebmann and Smith 1996). Specifically, the grid precipitation of the CRA-40/Land dataset (Liang et al. 2020) with 0.5° × 0.5° grid in China is used to avoid the uneven spatial distribution of station data. The precipitation form CRA-40/Land dataset has introduced two sets of observation based global precipitation analyses, which are CPC Merged Analysis of Precipitation (CMAP; Xie and Arkin 1997) and CPC unified daily gauge analysis (CPCU; Xie et al. 2007), and blended them with the CRA-40 reanalysis precipitation. Therefore, the precipitation from CRA-40/Land dataset is highly consistent with other rain gauge-based gridded dataset in China, such as CN05.1 (Wu and Gao 2013). All the observational data cover the period of 1981–2019.

## 2.3 Methodology

A pentad mean is applied to remove synoptic-scale disturbances, with 6 fixed pentads for one month and 72 pentads for one year. Then, to obtain the anomaly of each pentad, the climatologic annual cycle is removed by subtracting a climatological 18-pentad low-pass filtered component, while the climatology is defined as the 30-year average of 1981–2010. Note that for the hindcast data, the pentad mean is calculated from the average of the latest 2 forecasts from the initial date, and the model climatology is a function of both the initial calendar date and lead time.

Because the distinct variation characteristics in different regions, it is necessary to divide the entire China domain into several subregions that share spatially coherent variability. Here, K-means cluster analysis (Kaufman and Rousseeuw 2009) was used to objectively classify the subregions for boreal winter (NDJFMA) and summer (MJJASO) extended seasons. As shown in Fig. 1, seven subregions [from Region 1 (R1) to Region 7 (R7)] may be appropriate for the divisions: northeast China (NEC), north China (NC), Yangtze-Huaihe River Basin (YH), south China (SC), southwest China (SWC), Tibetan Plateau (TP), and northwest China (NWC). Compared with winter, the slight differences in the

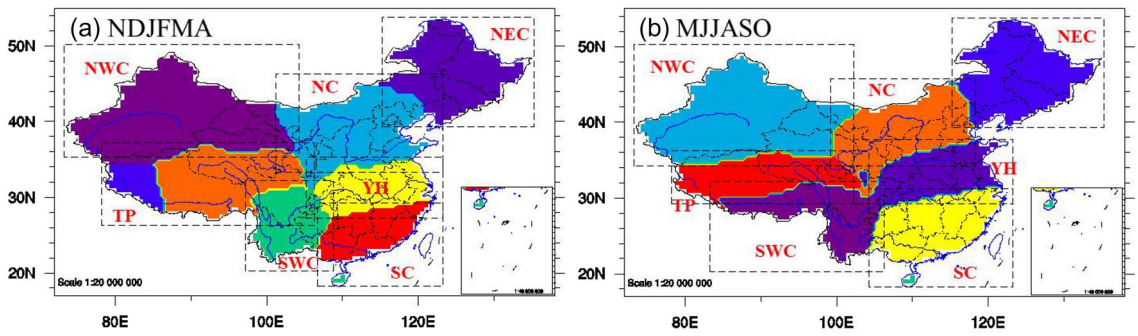


**Fig. 1** Divisions of China for **a** expanded boreal wintertime (NDJFMA) and **b** summertime (MJJASO) based on the K-means cluster analyses of subseasonal rainfall anomalies

divisions in the summer half-year mainly lay on the expansion of the SWC and SC regions, which may be attributed to the northward advance of the southwest summer monsoon. Therefore, seven rectangular domains for each region (Tables 1 and 2) are defined, and the prediction results for the overlap sectors are the average of both involving regions to ensure a smooth transition across the regions when combining the forecasts of subregions into the entire China.

A dynamical-statistical prediction model (DSPM) is proposed to improve the original dynamical model forecast in this study. The major procedures to construct the model are shown in Fig. 2 and can be described as follows. (1) Extended-singular value decomposition (E-SVD). For each subregion, simultaneously consecutive 6-pentad data of predictor and predictand are used for the E-SVD so that the temporally coupled evolving patterns are extracted for predictor and predictand. (2) Linear Regression. A linear regression relationship is built according to the time series of observed predictor and predictand. (3) Projection. the dynamical prediction of each predictor is used for projection to obtain the time series of predictors, which are further plugged into the regression equation to calculate the predictand time series. (4) Reconstruction. Prediction can be made by multiplying the reproduced time series by the predictand modes. Finally, the prediction should be modulated by multiplying the amplification factors that are determined by the amplitude ratios between observation and DSPM original prediction during the training period.

The temporal correlation coefficients (TCCs) and the spatial anomaly correlation coefficients (ACCs) are used as skill metrics for verifying precipitation forecasts. All of the time correlation verification of precipitation forecasts are based on pentad data, and effective sample size is estimated following Chen (1982) to determine the significance threshold of TCC skills. The significance of the TCC differences was examined using Steiger's *Z*-test (Raghunathan et al. 1996).

**Table 1** Details of the 7 subregions and their corresponding predictors in MJJASO

| Region | Geographic areas | Domains | Predictor domains | Predictors |
|---|---|---|---|---|
| R1 | Northeast China (NEC) | 115.25° E–135.25° E; 39.25° N–53.75° N | 60° E–180° E; 20° N–80° N | SH700, U850, H200, H850 |
| R2 | North China (NC) | 99.25° E–118.25° E; 34.25° N–45.75° N | 40° E–160° E; 0° N–70° N | SH700, SLP, U200, U850, H200, H850 |
| R3 | Yangtze-Huaihe River Basin (YH) | 102.25° E–123.25° E; 29.25° N–37.75° N | 40° E–160° E; 10° S–60° N | OLR, SLP, U200, H850 |
| R4 | South China (SC) | 104.25° E–123.25° E; 18.25° N–31.25° N | 60° E–160° E; 20° S–50° N | OLR, U200, U850, H500, H850 |
| R5 | Southwest China (SWC) | 83.25° E–106.25° E; 20.25° N–32.25° N | 20° E–140° E; 20° S–60° N | OLR, SH700, U200, H200, H850 |
| R6 | Tibet Plateau (TP) | 78.25° E–104.25° E; 29.25° N–36.25° N | 20° E–130° E; 0° N–70° N | OLR, SH700, U200, U850 |
| R7 | Northwest China (NWC) | 73.25° E–102.25° E; 34.25° N–50.25° N | 20° E–130° E; 10° N–70° N | OLR, SH700, U850, H200 |

**Table 2** Same as Table 1, but for NDJFMA

| Regions | Geographic areas | Domains | Predictor domains | Predictors |
|---|---|---|---|---|
| R1 | Northeast China (NEC) | 115.25° E–135.25° E; 39.25° N–53.75° N | 60° E–180° E; 10° N–70° N | OLR, U850 |
| R2 | North China (NC) | 101.25° E–123.25° E; 33.25° N–46.25° N | 40° E–160° E; 0° N–60° N | OLR, SH700, U850 |
| R3 | Yangtze-Huaihe River Basin (YH) | 105.25° E–123.25° E; 27.25° N–35.75° N | 40° E–160° E; 10° S–60° N | OLR, SH700, U850 |
| R4 | South China (SC) | 106.75° E–123.25° E; 18.25° N–29.25° N | 40° E–160° E; 20° S–40° N | OLR, SH0700, SLP, U850, H850 |
| R5 | Southwest China (SWC) | 97.25° E–108.25° E; 20.25° N–32.25° N | 20° E–140° E; 20° S–50° N | OLR, U850 |
| R6 | Tibet Plateau (TP) | 78.25° E–106.25° E; 26.25° N–37.25° N | 20° E–140° E; 20° S–60° N | OLR, SH700, H200 |
| R7 | Northwest China (NWC) | 73.25°E–104.25° E; 35.25° N–50.25° N | 20° E–140° E; 0° N–70° N | SH700, H200, H500 |

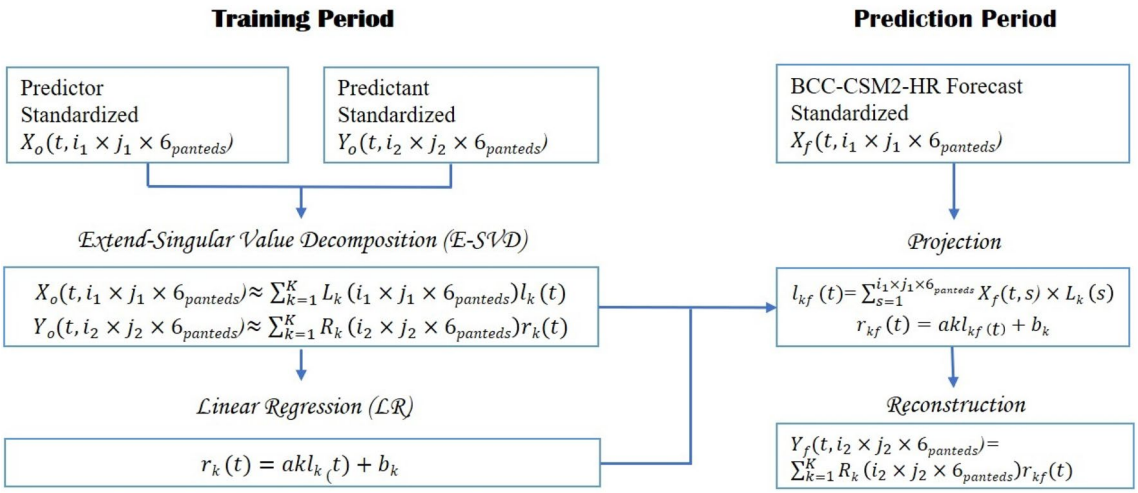


**Fig. 2** The diagram of major steps of DSPM. *X* and *Y* are normalized predictor and predictand, respectively. *i* and *j* denote spatial grids for the predictor and predictand, *t* is time. *K* is the total number of SVD modes. $L_k$ and $R_k$ denote the singular vectors of predictor and predictand, respectively. $l_k$ and $r_k$ indicate the time series of expansion coefficient of the kth SVD mode for the predictor and predictand, respectively. $a_k$ and $b_k$ indicate the coefficient and constant of the regression equation. The subscripts "o" and "f" represent observation and forecast. See the text for more information

The MJO and BSISO prediction skill can be measured by the bivariate anomaly correlation coefficient (COR, Gottschalck et al. 2010). Single-member predictability is calculated by the COR between one ensemble member and the rest of the members and averaged over all subsamples, while ensemble predictability is measured in the same way but between one ensemble member and the mean of the remaining members (Kim et al. 2014).

## 3 Evaluation of BCC model direct prediction

### 3.1 Climatology

The evolution of the climatological rain belt over eastern China in the BCC model is evaluated for forecasts at different lead pentads. Generally, the forecasted rainfall belt along 105°–120° E shows consistent features with the observation for the short lead time, which is characterized by a northward shift after the onset of the South China Sea summer monsoon in late May, reaching northern China in late July and retreating southern China in September (Fig. 3). However, the model biases increase with lead time, as indicated by the ACC decreasing from 0.87 to 0.75 for forecasts of 1–6 pentads. The main deviations lie on the underestimated precipitation during the preflood season in the southern China and the Meiyu period in the Yangtze River basin after the 3-pentad forecast, and there are overestimations of the northward movement of the rain belt in northern China and precipitation over the second flood season in southern China.

### 3.2 Prediction skills of subseasonal precipitation in China

The TCC skills of pentad rainfall anomalies predicted by the BCC model over China are shown in Fig. 4. The useful skills basically persist for approximately 3 pentads in most regions, and the relatively higher skills are mainly located in southern China and the eastern TP. After 4 pentads, the model nearly loses its skill over all of China except south of the Yangtze River, with the areally averaged TCC skills over all of China dropping below 0.1. Notable that the prediction skills are relatively higher over eastern Tibetan Plateau (ETP), consistent with the model's good performances on its local mid-level geopotential height anomalies, which may relate to the higher predictability over the tropical Indian Ocean through a meridional teleconnection (Fig. S1).

The skill dependences on the annual cycle are given in Fig. 5 for each region. In the climatic sense, the prediction skills are relatively higher during the extended boreal winter than summer, especially in February–March and October–November, with the useful skills extending up to 4–5 pentads over some regions (such as NC, YH, and SC). Note that the lowest skills appear in August over the YH and SC regions, presumably associated with their larger climatological biases at the time (Fig. 3).

### 3.3 Prediction skills for atmospheric circulation

Compared with rainfall, circulation forecasts are typically much more reliable in the model. Figure 6 shows the skills of the 850-hPa stream function, which represents the large-scale

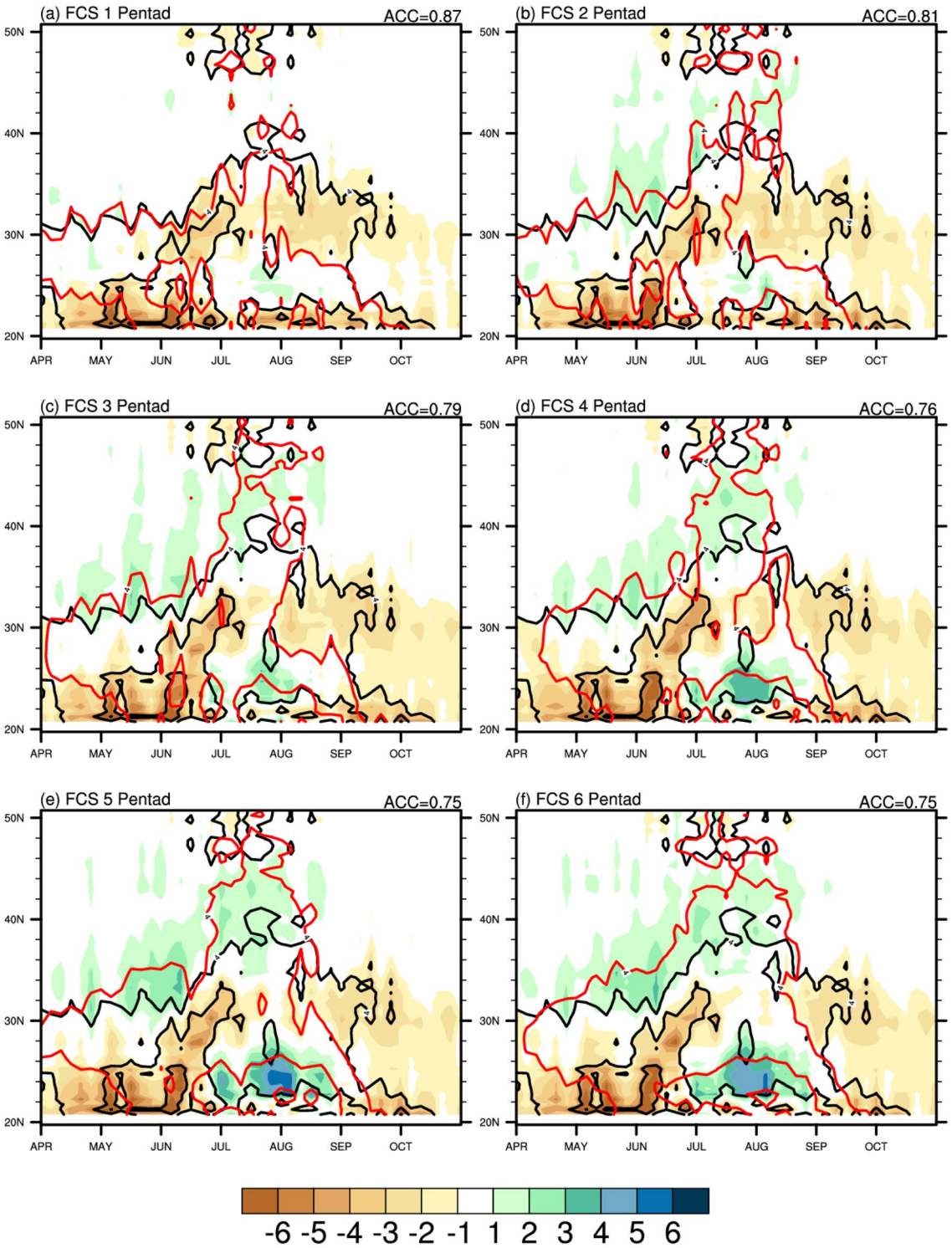


**Fig. 3** The climatological time-latitude cross-sections of pentad precipitation (mm day$^{-1}$) with an average of 105°–120° E from April to October for observations (black lines), BCC models (red lines) and their differences (shadings). The contours denote rainfall at 4 and 8 (mm day$^{-1}$). **a**–**f** Show the forecast time of 1–6 pentads. The spatial anomaly correlation coefficients (ACCs) between the observations and model forecasts are given in the upper-right corner of each panel

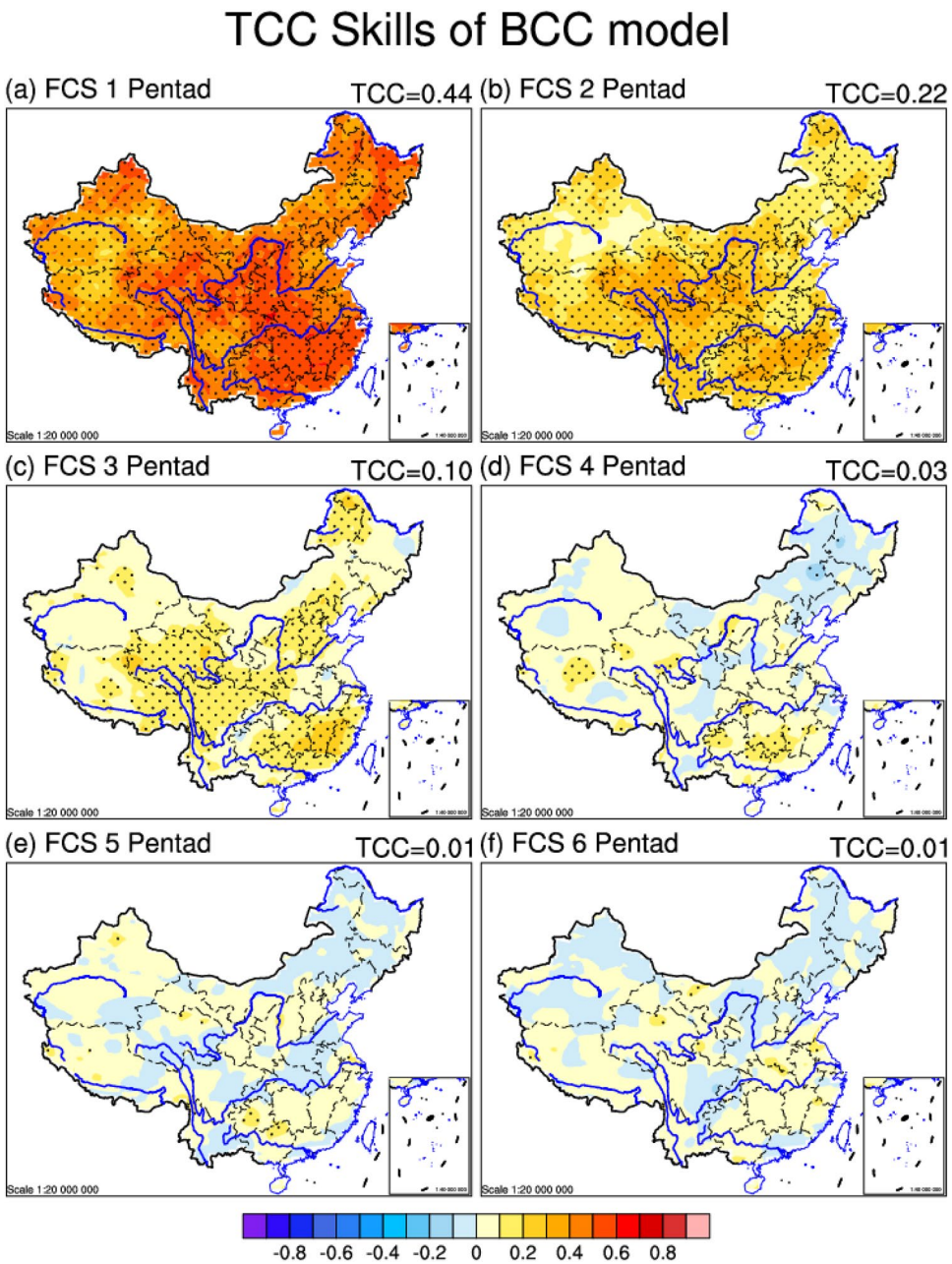


**Fig. 4** TCC skills for pentad precipitation predictions in BCC model over China during 2005–2019. **a**–**f** Show the forecast time of 1–6 pentads, where the stipples denote where the TCCs skill are statistically significant at the 95% confidence level. The TCC skills averaged over China are given in the upper-right corner of each panel

rotational component of low-level circulation. The TCC is higher than 0.7 for the first 2 pentads worldwide except for the African continent. The skills drop slowly with increasing forecast time but still pass the significance level up to 6 pentads over East Asia, the tropical Indian Ocean, and the tropical Pacific. The predictability sources mainly come from the realistic circulation responses to convection anomalies over the tropical Indian Ocean-west Pacific (IOWP) warm pool (Fig. S2), which are associated with MJO and ENSO (Andrade et al. 2019). However, the convection signals are mainly confined within IOWP warm pool areas and dissipated sooner after reaching Western Hemisphere, which may contribute to the relatively lower prediction skills of circulation over the African continent. Therefore, the skill of precipitation prediction may be improved by constructing a reasonable dynamical-statistical model, which could take full advantage of the skillful circulation prediction by the dynamical model and the stable circulation-precipitation relationship by statistical methods.

## 4 The dynamical-statistical prediction

### 4.1 The establishment of the DSPM

Several candidate predictors for precipitation prediction are selected according to some previously revealed physical

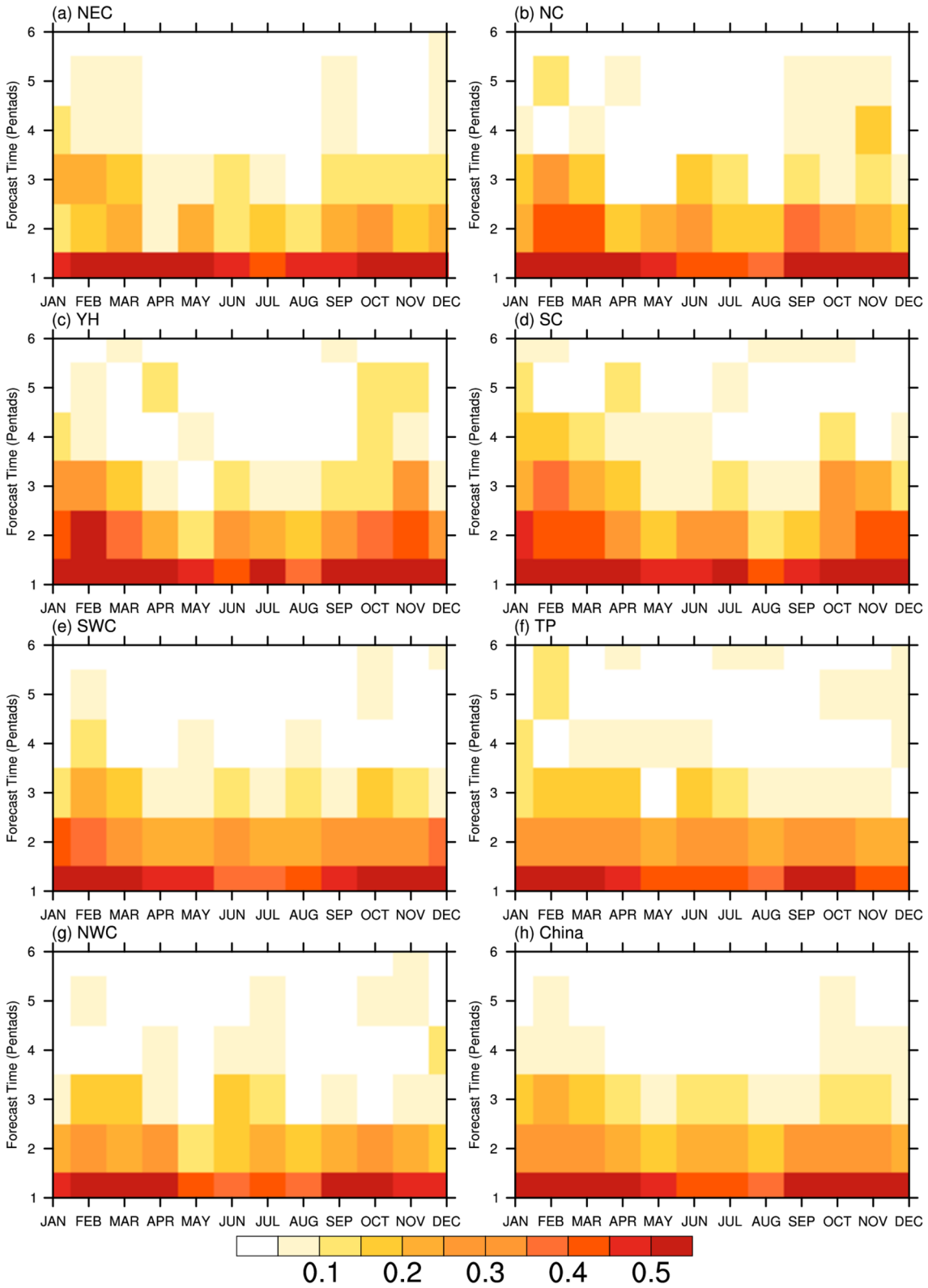


**Fig. 5** The averaged TCC skills of pentad precipitation predictions in BCC model for each month. **a**–**h** Show the NE, NC, YH, SC, SWC, TP, NWC and all of China

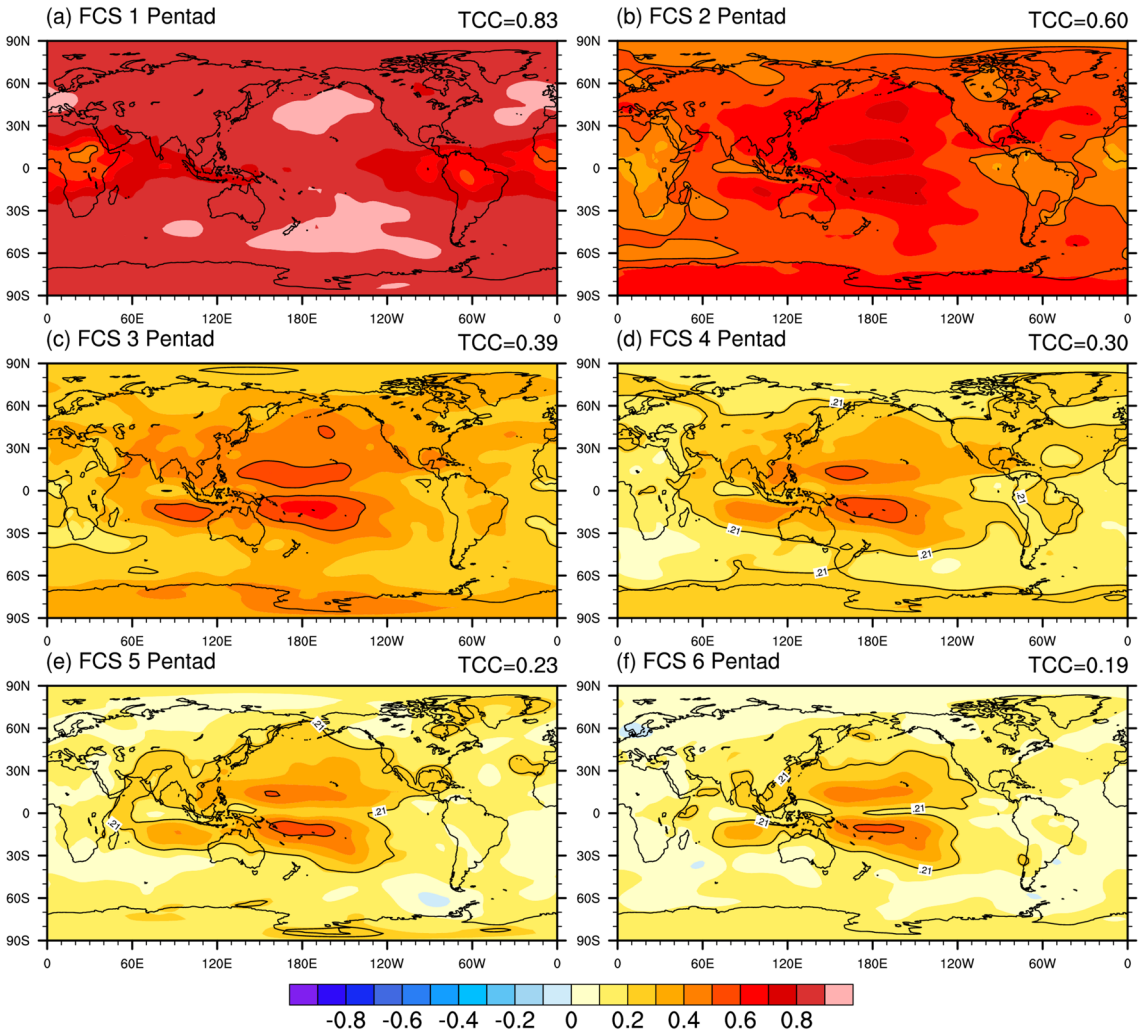


**Fig. 6** TCC skills for the pentad 850-hPa stream function prediction in BCC model during 2005–2019. **a**–**f** Show the forecast time of 1–6 pentads, and the black contours show the TCC skills of 0.21 and 0.5, while the 0.21 is TCC criterion of statistically significant at the 95% confidence level. The area-averaged TCC skills over the Eurasian-Pacific domain (40º–180º E, 20º S–70º N) are given in the upper-right corner of each panel

mechanisms (Zhu and Li 2017). The OLR, 850-hPa and 200-hPa zonal winds (U850 and U200) are selected as potential predictors since the MJO signal can be well captured by their combination (Wheeler and Hendon 2004). U850 and U200 could also represent activities of the western Pacific subtropical high (WPSH) and upper-level westerly jet, respectively. The geopotential heights at 850, 500 and 200 hPa (H850, H500, and H200) are also selected to represent the activity of the WPSH and South Asian high (SAH). The specific humidity at 700 hPa (SH700) is used given its slowly varying nature and important impacts on the development of the MJO (Hsu and Li 2012). In addition, SLP is a good indicator of air mass variability and can directly influence precipitation variation (Liu et al. 2021b).

Domains of the predictors in different regions are determined by their lead-lag correlation patterns against the region-averaged rainfall index (figures omitted). Generally, for the northern regions of China (NEC, NC, and NWC), the correlated signals are mainly located over the upstream Euro-Asian continent and exhibit eastward propagation; however, for the southern regions of China (YH, SC, SWC, and TP), the combined effects from both the mid-high latitude and tropical signals are important. The details of the selected predictor and predictand and their domains for different regions are listed in Tables 1 and 2 for the extended season of summer and winter. The predictions in each region are the average of the results of every selected predictor, and the predictions of the overlapping areas are the average in each involved region.

E-SVD is applied to the simultaneously consecutive 6-pentad data of each predictor-predictand pair to extract their temporally coupled evolving patterns. Figure 7 shows

the first leading E-SVD modes for the pentad U850 (OLR) with precipitation anomalies in the SC region (R4) during the extended winter, which explains 21.0% (16.2%) of the squared covariance, and the correlation between the time series reaches 0.66 (0.61). As the eastward-propagating inactive convection and east wind anomalies from tropical Indian Ocean to the western Pacific, the precipitation anomalies in SC clearly experience a transition from a dry to wet phase during 6 pentads. This pair of temporally coupled patterns reflects the MJO modulation of the rainfall anomaly in SC, with more (less) precipitation occurring during Phases 2–3 (5–6) of the MJO, as revealed in previous studies (Jia et al. 2011; Li 2014). In addition to tropical signals, it also can be found that the rainfall anomalies over SC are influenced by the southward propagating circulations from mid-latitude during boreal winter.

Similarly, the leading E-SVD modes for the U850 (OLR) with rainfall anomalies in the SC region (R4) during the summer half-year are shown in Fig. 8, which explains 14.8% (15.7%) of the squared covariance, and the time correlation reaches 0.61 (0.64). Compared with winter, the rainfall anomaly over SC during summer is mainly influenced by the zonally elongated meridional wave train that originates from the Maritime Continent and propagates northward into central China. When the low-level westerly (easterly) wind is dominant, there will be more (less) precipitation over SC. These features are tightly associated with the activities of BSISO (Hsu et al. 2016), with a correlation coefficient between the E-SVD time series and the BSISO1-1 index defined by Lee et al. (2013) of − 0.57 for the period of 1981-2010 MJJASO. Therefore, the simultaneously consecutive E-SVD between the predictor and predictand can well capture some dominant predictability sources and their influences, which sets a solid basis for further dynamical-statistical combination prediction.

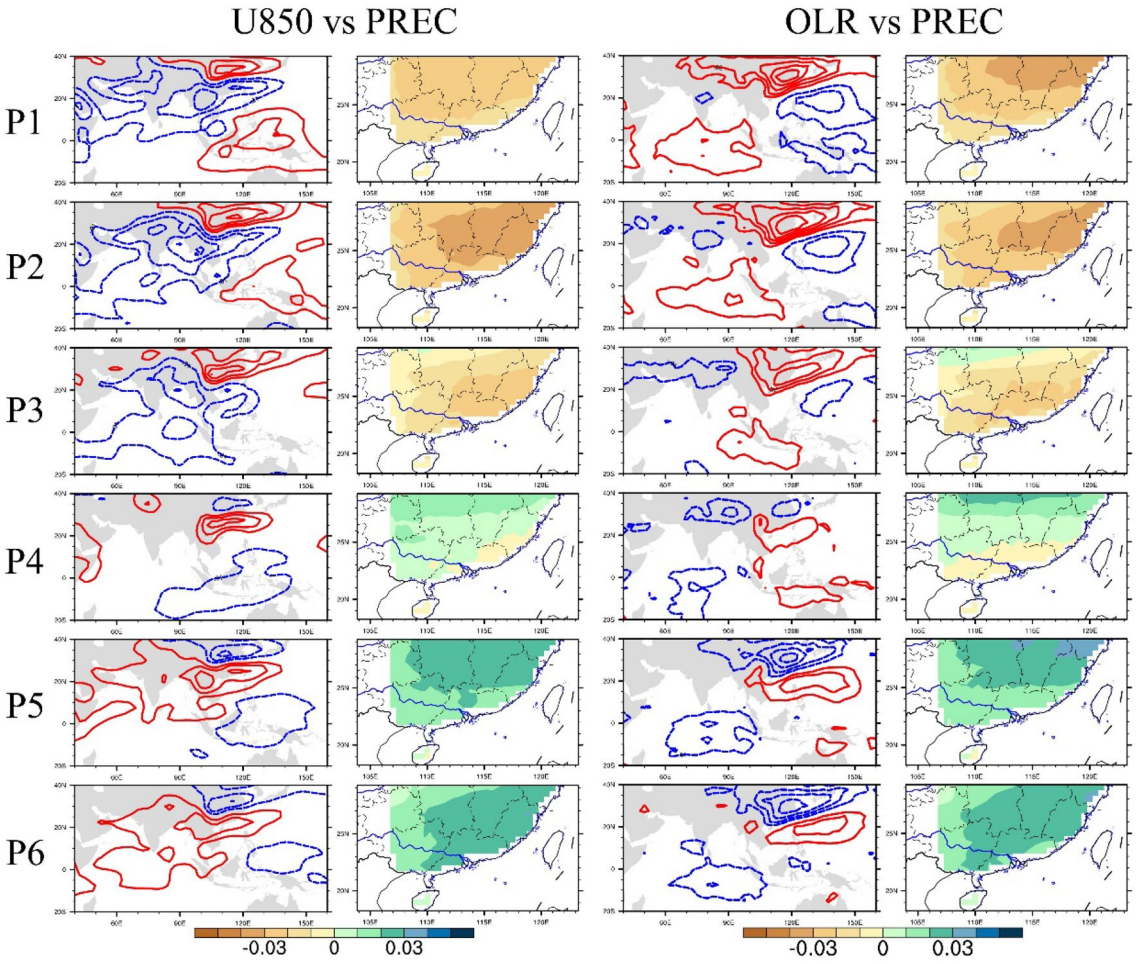


**Fig. 7** Patterns for the extended singular vectors of the first leading SVD for the U850 (left 2 columns) and OLR (right 2 columns) with precipitation in the SC region during NDJFMA

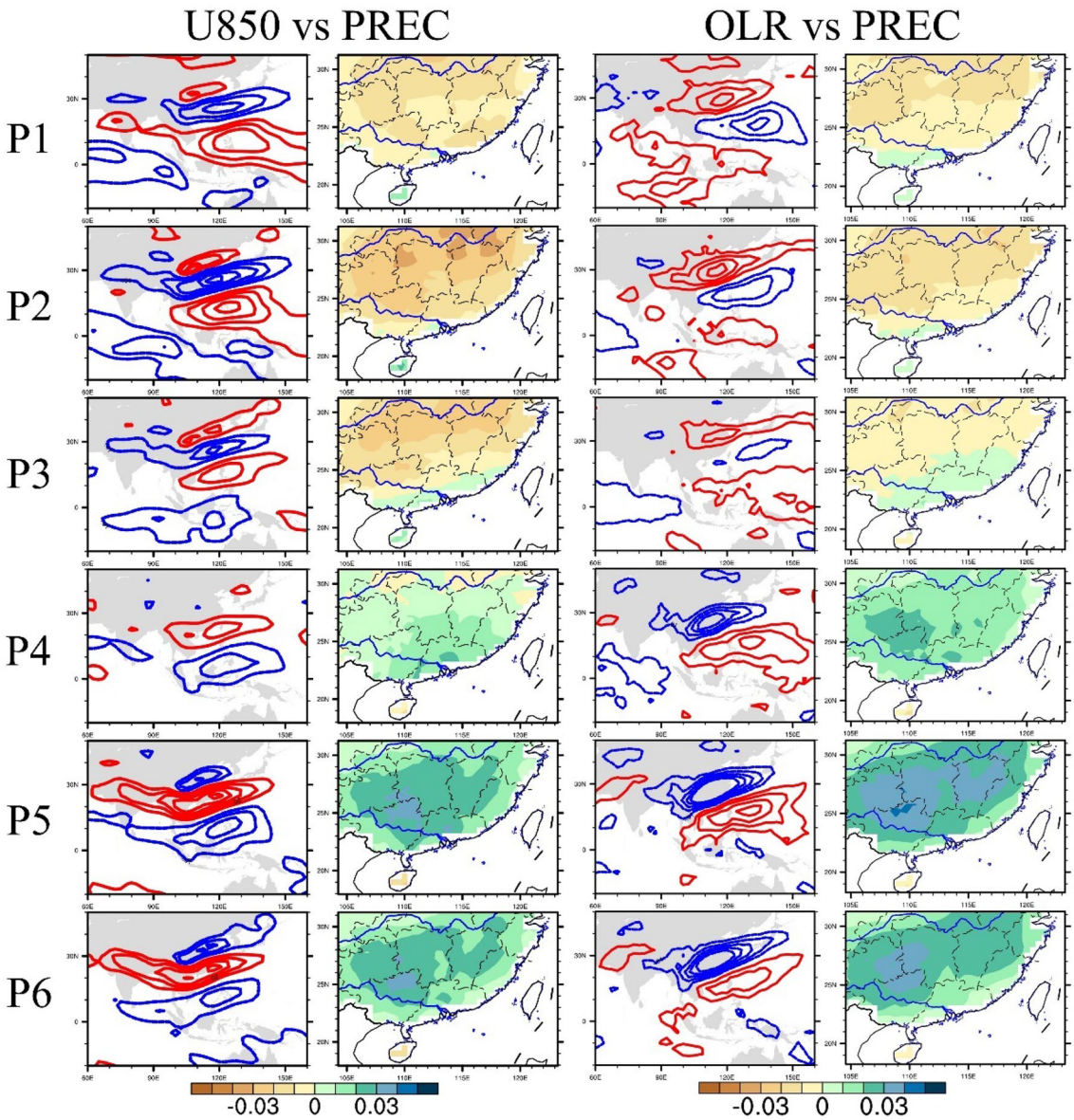


**Fig. 8** Same as in Fig. 7 but for MJJASO

### 4.2 Validation of the DSPM

Here, the first 10 leading SVD modes are retained for the predictor projection and predictand (precipitation) reconstruction given that their total accumulated explained covariance generally reaches above 70% and the correlations between predictor and predictand basically remain above 0.5 for each region. A rolling independent validation was carried out during the period of 2011–2019. That is, for 2011 (2012), only the observational data of 1981–2010 (1981–2011) are used for the training model, and so on. Selections of the predictor for each region (Tables 1 and 2) can be determined by the area-averaged TCC skills during the hindcast period (2005–2010).

The area averaged TCC skills of both the DSPM and BCC model are given in Fig. 9. During the boreal summer, the skills of the DSPM are only lower than the original model prediction in the first pentad but generally become higher thereafter, especially for NC, YH and NWC. For each predictor, the OLR and SH700 generally outperformed the other predictors for most regions (except NC and NEC), indicating the importance of tropical convection and low-level moisture in subseasonal precipitation prediction. However, the skills of other predictors are diverse on different regions, as some predictors are particularly useful in specific regions, such as U200 for the YH and TP regions, which may be attributed to the strong modulation of the westerly jet over precipitation in those regions. During the boreal winter, the superiority

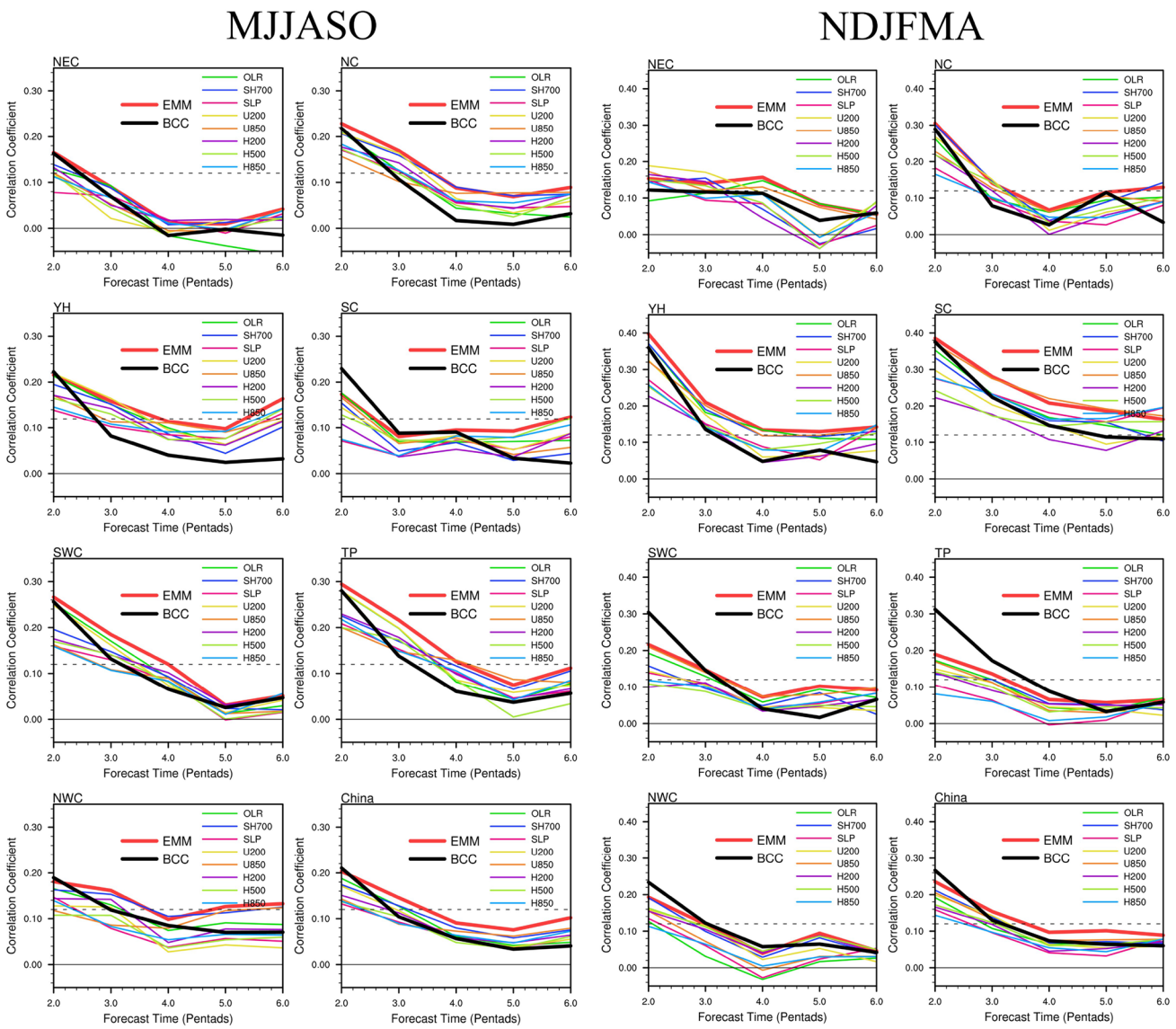


**Fig. 9** The area averaged TCC skills of pentad precipitation anomaly forecasts by the BCC model and DSPM during MJJASO (left 2 columns) and NDJFMA (right 2 columns) for each region. The solid thick black, red, and thin colored lines represent the skills of the BCC model, ensemble mean of the DSPM (denoted as EMM), and each predictor of the DSPM, and the dashed gray lines represent statistically significant correlations at the 95% confidence level. The regions are labelled at the upper-left corner of each panel, which are NE, NC, YH, SC, SWC, TP, NWC and all of China

of DSPM is obviously in the YH and SC region, which are mainly associated with the higher skills from the predictors of OLR and U850, indicating the potential contribution of MJO modulation. However, less skill's improvement can be found in the TP and NWC region, indicating regional differences exist for DSPM. Overall, the skills of the ensemble-mean (EMM) predictions for all the predictors are higher than those of each single predictor, showing the effectiveness of the multipredictor ensemble and the rationality of predictor selection. The TCC skills of regional mean pentad rainfall anomalies (Fig. S3) are generally highly than the averaged of TCC skills of each grid, since the regional mean acts as spatial average to extract large scale variability. The main conclusion still stands that the DSPM also out-perform than BCC model over most regions with the similar skill's improvements.

Figure 10 show the distributions of the TCC skills over China for the DSPM and their differences from the BCC model. In general, the skill descending as the lead time is much slower in the DSPM, which can maintain skillful prediction over 6 pentads for the central China, YH, Jiangnan and NWC regions during boreal summer and for the north China and South China during boreal winter. From the forecast time of 3 pentads, the DSPM is superior to the

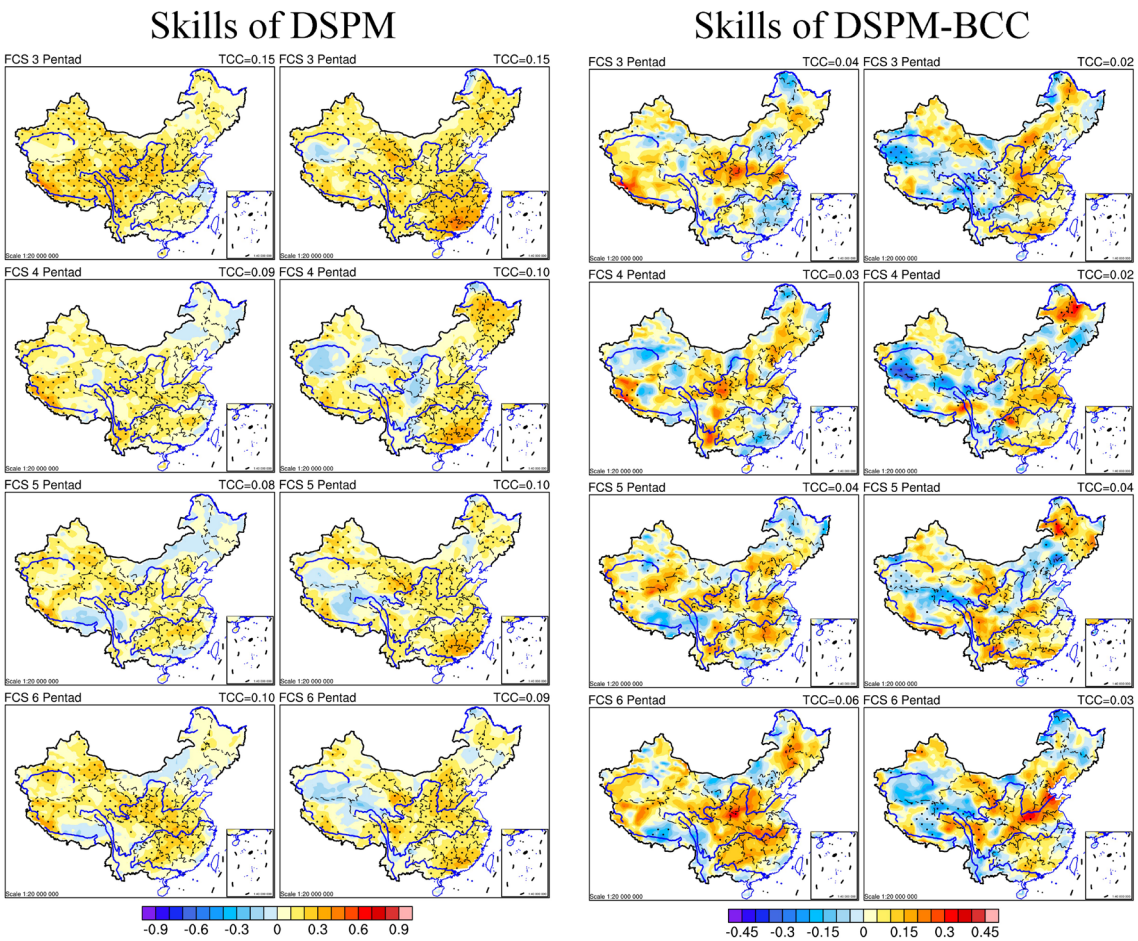


**Fig. 10** TCC skills of the DSPM (left 2 columns) and the skill differences between the DSPM and BCC model (right 2 columns) during 2011–2019 MJJASO (the 1st and 3rd columns) and NDJFMA (2nd and 4th columns). The 1st to the 4th rows show the forecast time of 3–6 pentads. The stipples denote where the TCC skills or the skill differences are statistically significant at the 95% confidence level. The skills or the skill differences averaged over China are given in the upper-right corner of each panel

BCC model over most regions and becomes even larger as the forecast time increases. Notably, the skills of the DSPM over NEC, SWC and coastal SC during boreal summer and over west China during boreal winter are relatively lower than other regions. These differences may be attributed to precipitation variability over those regions are largely influenced by mid-latitude factors, orographic precipitation and landing tropical cyclones, respectively, both of which are difficult to be captured by DSPM on subseasonal timescales. In addition, the ACC skills of the BCC model and DSPM also reflect the higher skills of the DSPM after 2–3 pentads, especially for the YH, TP and NWC regions.

A typical case study for the real-time prediction of the record-breaking rainfall event over the Yangtze River Basin in June 2020 (Liu et al. 2020) is shown in Figs. S4–S5. The forecast initialized on 1st June in the DSPM steadily captured the rain belt over the mid-lower reaches of the Yangtze River, with the ACC skills sustained at approximately 0.3 for 6 pentads, while the skills of the BCC model dramatically decreased to below 0 after 4 pentads.

## 5 Predictability source analysis

### 5.1 Predictability of the MJO and BSISO

The potential predictability sources for the subseasonal prediction in the DSPM and BCC model are analyzed in this section. Generally, because of their regular activity nature and significant modulations of precipitation anomalies (as shown in Figs. 6 and 7), both the MJO and BSISO are well recognized as the major predictability sources for subseasonal prediction. Therefore, it is valuable to examine the predictability of the MJO and BSISO in the BCC model and their possible effects on subseasonal prediction skills.

The prediction skill and the predictability of the RMM and BSISO index as a function of lead time in the BCC

model are shown in Fig. 11. During the boreal winter, the single-member and ensemble-mean prediction can achieve useful RMM skills up to 20 and 23 days in advance, respectively, when taking the corresponding COR beyond 0.5 as the threshold. Such an increased skill level, compared with the previous version of the BCC model (Liu et al. 2017), is still lower than the potential predictability limit, which can reach up to ~ 35 days in terms of single-member estimation and ~ 40 days in terms of ensemble-mean estimation. During the boreal summer, the prediction skill and predictability of the RMM index become slightly shorter (Fig. 11b), with approximately 19 and 22 days for the single-member and ensemble-mean predictions, respectively. For the BSISO index (Lee et al. 2013), as seen in Fig. 11c, d, the number of useful forecast days can reach 12–13 days and 10 days for BSISO1 and BSISO2, respectively, and their corresponding predictability limits can extend to 28–38 days and 23–29 days, respectively, which may be related to their intrinsic oscillatory periods (30–60 days and 10–30 days). We also check the model performance on MJO (denote as MJO-K12) and BSISO (BSISO-K12) index defined by Kikuchi et al. (2012) and the ROMI index (ROMI-K14) define by Kiladis et al. (2014), which represent more coherent propagation characteristic of MJO and BSISO (Wang et al. 2018). Consistent with recently studies (Wang et al. 2019; Shibuya et al 2021), it is found that (Fig. S6) the prediction skill can reach up to 37 and 29 days for MJO-K12 and ROMI-K14 index during boreal winter, 30 days and 24 days for BSISO-K12 and ROMI-K14 index during boreal summer, respectively, which are higher than the traditional RMM and BSISO indices. Therefore, compared with the direct precipitation prediction, the dynamic BCC model is more capable of capturing these major modes of subseasonal variability.

## 5.2 Effects of the MJO and BSISO on prediction skills

Figure 12 presents the scatter plots of the prediction skills when initialized with a strong versus weak MJO or BSISO event (the amplitude of the RMM or BSISO index is larger or smaller than 1, respectively) in the DSPM. The marks above the diagonal line indicate that the skills are higher for predictions initialized from the strong MJO or BSISO events compared with weak ones. During the wintertime, the DSPM forecasts for pentads 1–5 show overall consistently higher skills with a strong MJO at the initial time, with the China-averaged skill marks basically located above the diagonal line. Except for NEC and NWC, the positive effects of the MJO exist in most regions of China where

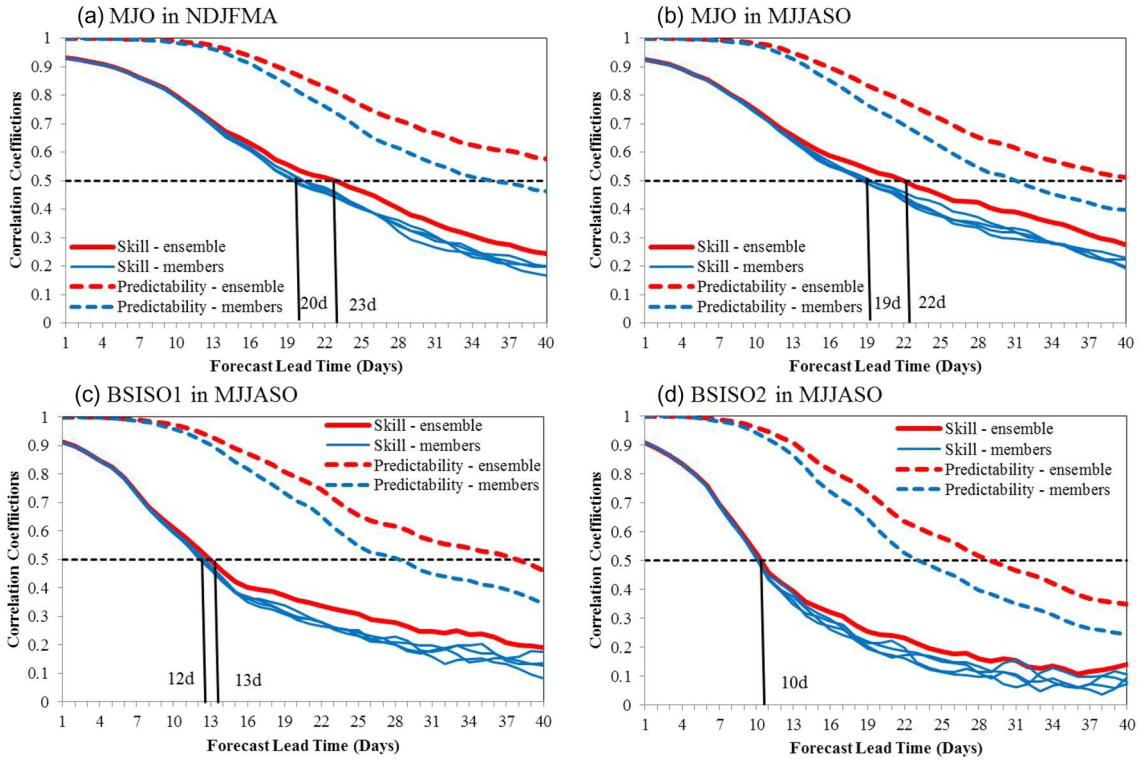


**Fig. 11** Predictability (dashed lines) and prediction skill (solid lines) of the **a**, **b** RMM and **c**, **d** BSISO index as a function of the lead time for the period of **a** NDJFMA and **b**, **c**, **d** MJJASO in the BCC model. The blue and red lines represent the prediction skills and predictability of ensemble members and ensemble mean. The horizontal dashed lines are 0.5

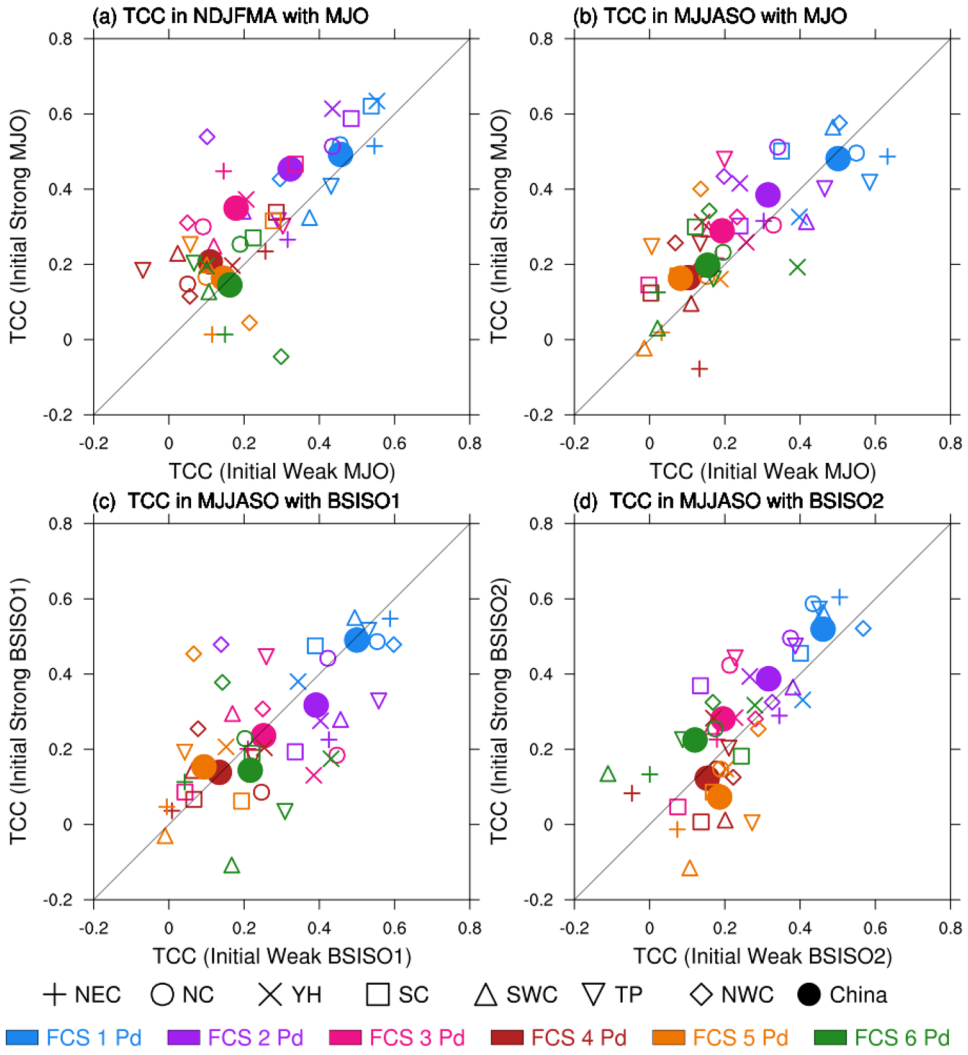


**Fig. 12** Scatter plots for the area-averaged TCC skills of each region in the DSPM. The *X*-axis (*Y*-axis) represents the prediction skill of the forecast initialized with strong (weak) MJO (**a**, **d**) and BSISO (**c**, **d**) conditions. The validation time is for NDJFMA (**a**) and MJJASO (**b**, **c**, **d**). The forecast pentads are denoted by different colors, and the regions are denoted by different marks

the MJO signals are considered potential predictors (i.e., the OLR and U850 over the equatorial Indian Ocean and western Pacific area are selected as predictors). During the boreal summer, most of the regions have higher skills when initialized from a strong BSISO2 event, especially for NC, YH, SC and TP, where the related predictors mainly cover the signals of convection and circulation over the Wester Pacific and Maritime Continent. Therefore, the prediction skills of the DSPM are very likely dependent on the initial states of some well-known predictability sources. In addition, the modulations of MJO and BSISO on prediction skill can also be found in BCC model (Fig. S7), but with smaller skills improvements.

Figure 13 shows a direct comparison of the effects of the MJO on predictions of the DSPM and BCC model, where the marks above the diagonal line indicate that the skills are higher in the DSPM than in the BCC model. Moreover, the solid and hollow marks in Fig. 13 denote the forecasts initialized with a strong and weak MJO, where if the solid marks move to the up (right) of the hollow marks, the corresponding predictions would have higher skills when initialized with the MJO in the DSPM (BCC model). For all of China (Fig. 13h), both models show that the predictions with strong MJO initialization are more skillful for the forecast time of pentads 1–4, indicated by the solid marks shifting to the upper and right sides relating to the corresponding hollow marks. More importantly, the better performance of the DSPM mainly appears when the forecasts have been initialized from the strong MJO, shown by the more solid marks located above the diagonal line than the hollow ones, especially over the YH, SC and SWC, implying that the superiority of such a dynamical-statistical model can mainly be attributed to its capability of better capturing the realistic influences of those major predictability sources.

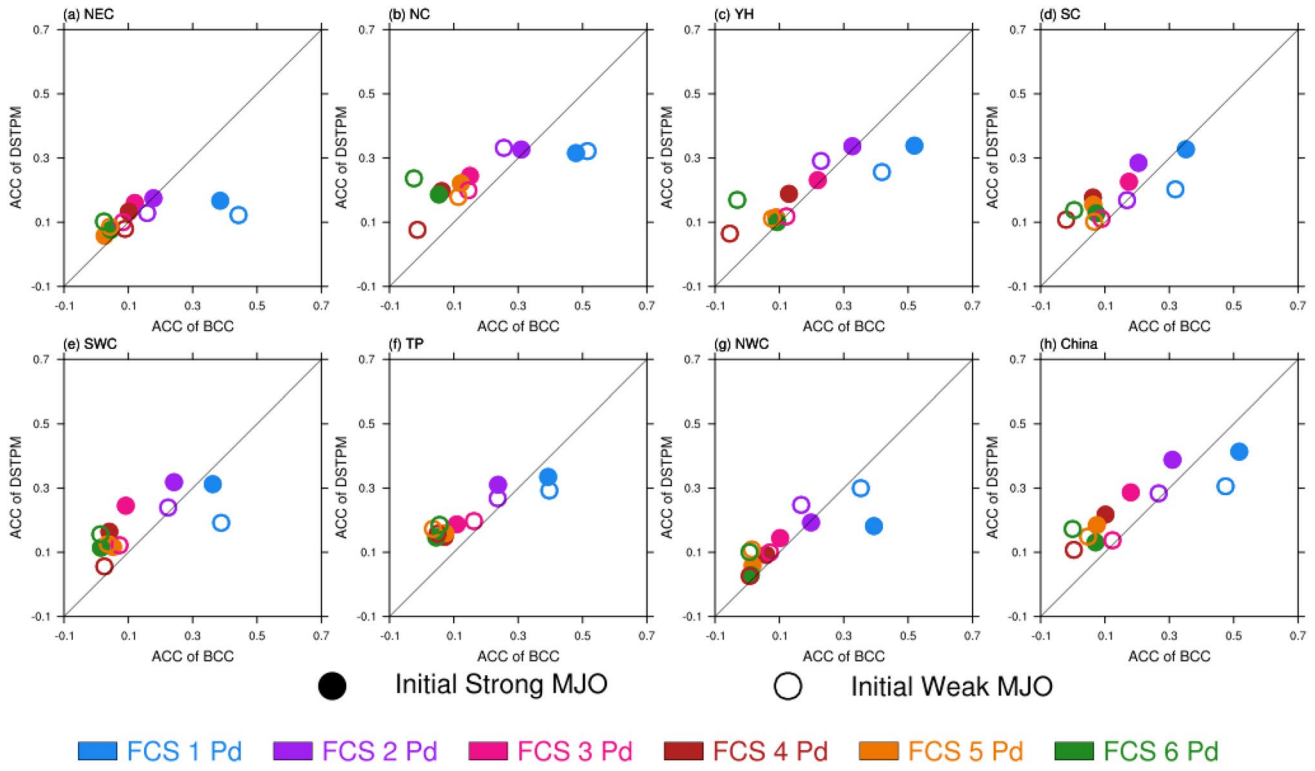


**Fig. 13** Scatter plots for the ACC skills of each region. The *X*-axis (*Y*-axis) represents the prediction skill of the BCC model (DSPM). The solid (hollow) circles indicate the forecasts initialized with strong (weak) MJO conditions. The validation time is NDJFMA, and the forecast pentads are denoted by different colors. **a**–**h** Denote the regions of NE, NC, YH, SC, SWC, TP, NWC and all of China

## 6 Summary and discussion

In this study, the prediction skills of the BCC new-generation S2S operational model for pentad precipitation and circulation anomalies are verified. Then, based on the extraction of simultaneously coupled evolving patterns between precipitation and its atmospheric circulation predictors, a dynamical-statistical prediction model, denoted as the DSPM, was constructed to improve the original prediction of the BCC model. Finally, as the major predictability sources at the subseasonal timescale, the potential effects of the MJO and BSISO on the prediction skills of the BCC and DSPM are revealed.

The BCC model can generally capture the climatological rain belt evolutions over eastern China, although some deficiencies still exist, such as the unrealistic weaker Meiyu front, the stronger second flood season in SC, and the excessive northward shifting of the rain belt, which become larger as the forecast lead time extends. However, the skillful predictions of pentad precipitation anomalies are mainly confined within 3 pentads over most regions of China, with even lower skills during boreal summer. In comparison, the predictions of circulation variables are more reliable, especially over the East Asian and west Pacific areas, providing the possibility for further dynamical-statistical correction forecasts.

Based on the K-means analysis of pentad precipitation anomalies, all of China is divided into 7 subregions for summer and winter. By applying E-SVD to the temporally coupled evolving patterns of the predictors and predictands, the DSPM that effectively captures the modulation of the major subseasonal variability (such as the MJO and BSISO) on precipitation was built for each region. The independent validation results show that the prediction skills of precipitation anomalies are generally improved by the DSPM after a forecast time of 3 pentads, especially for the NC, YH, SC and part of the NWC regions, where the skillful prediction can persist for 6 pentads.

For major subseasonal variability, the prediction skills of the MJO and BSISO reach approximately 22–23 days and 10–13 days in the BCC model, respectively, both of which are largely improved compared with the previous version (Liu et al. 2017; Jie et al. 2017). In the DSPM and BCC models, the overall prediction skills of precipitation tend to be higher when the forecasts are initialized with a strong MJO at pentads 2–5 during winter and with a strong BSISO2 at pentads 1–4 during summer, confirming that the MJO and BSISO are important predictability sources for subseasonal prediction. Moreover, the skill improvements in the DSPM

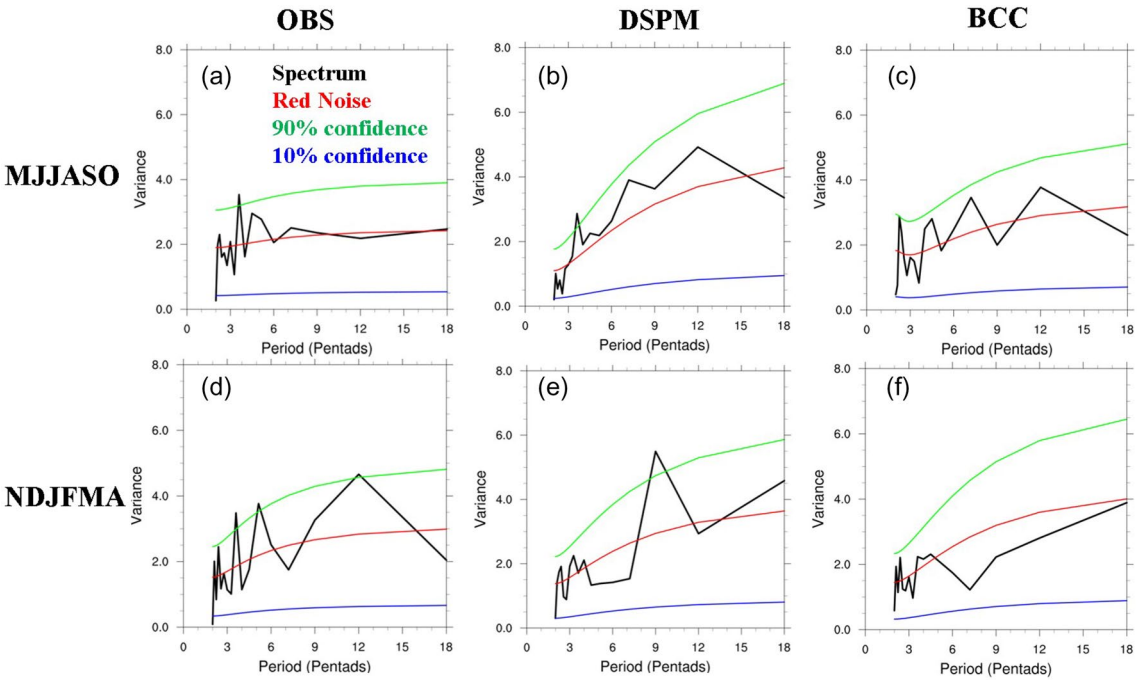


**Fig. 14** Power spectrum of pentad rainfall anomaly averaged over South China (SC) for the **a**, **d** observation and 3-pentad lead forecasted by **b**, **d** DSPM and **c**, **f** BCC model during **a**–**c** MJJASO and **d**–**f** NDJFMA. The black, red, green and blue lines denote the power spectrum, the Markov "red noise" spectrum, and the threshold of the 90% and 10% confidence levels, respectively

are larger than those in the BCC model when initiated from the strong MJO over most regions of China (except NEC and NWC), indicating that the superiority of the DSPM may be attributed to the more realistic representation of the MJO and BSISO modulations over precipitation anomalies.

By using the same three predictors (OLR, SH700 and U850), the prediction skills of DSPM had been compared with that of a pure statistics model, which is STPM proposed by Zhu and Li (2017). The results show that except for NEC region, the DSPM generally displayed higher skills than the statistics model, especially during the first 3 pentads. Noted that the STPM we used here is not exactly same with that of Zhu and Li (2017) for the region division, predictor selection and period for verification, which may bring some discrepancies with their results.

It is worth noting that the DSPM does not perform well over the SC region during the boreal summer with the skills even lower than the dynamic model during the boreal summer (Fig. 9). This problem may attribute to the intrinsic nature of DSPM and the main periodicity of the rainfall variability over SC in summer. Since the E-SVD method is used to construct the prediction model, the DSPM is more capable of capturing the relatively low-frequency intraseasonal signal with the period of 6–15 pentads (30–90 days). However, except for slowly-varying MJO and BSISO, rainfall anomalies over SC could also be largely influenced by relatively high-frequency synoptic-scale weather systems (such as typhoon and tropical easterly wave) and quasi-biweekly oscillation, both of which could not be well captured by the DSPM. As shown in Fig. 14, the observed rainfall anomaly over SC has an obvious peak at about 2–4 pentads (10–20 days) but little power spectrum for the longer intraseasonal period, which are necessary for the good operation of DSPM. Compared with that, during the boreal winter (Fig. 14d–f), the rainfall anomalies over SC are mainly modulated by intraseasonal oscillation (such as MJO), which can be well captured by DSPM. As a result, the prediction skills of DSPM over SC are better compared to the BCC model forecast sooner after 2 pentads (Fig. 9). The spectra over other regions were also checked (figures omitted). Thus, we can infer that the prediction skills of DSPM are largely dependent on whether the prevailing of observed rainfall anomalies could be well described by the DSPM.

DSPM shows the degradation of prediction skill at short leads (1–2 pentads) compared to the dynamic model, which may attribute to the prediction strategy that consider the 6-pentad evolving pattern as a whole to extract the predictor signals. The prediction skills of the model with less pentads (e.g. 2 pentads) are truly slightly higher skill for the first 2 pentads, but decrease fast and become lower than the current model for the 3–6th pentads (Fig. S8), which is the mainly concerns of this study.

Since the DSPM we built in this study used the observed simultaneous consecutive 6-pentad data of the predictor and

predictand, the idealized prediction of the DSPM can be obtained if the forecasted predictors are replaced by the corresponding observational predictors, which could represent the potential predictability limit of this dynamical-statistical model. The results show that (Fig. S9) the idealized prediction can generally maintain the current skill level from pentad 1 to pentad 6 with no drop, showing that there is large room for potential improvement in subseasonal prediction for the DSPM model. Beyond that, the current study mainly focuses on the atmospheric circulation predictors which dynamic model has relatively higher skills. In the future studies, we will try to involve other important S2S predictability (such as land/soil processes, intraseasonal SST variability, troposphere-stratosphere interactions) in the proper way and utilize the deep learning method (Kim et al. 2021) to further improve the subseasonal prediction.

**Supplementary Information** The online version contains supplementary material available at https://doi.org/10.1007/s00382-022-06187-3.

**Acknowledgements** The computations were supported by the Advanced Computing East China Sub-center and the China Meterological Administration (CMA) Shuguang-PI high-performance computing platform and uses of the computational resources is gratefully acknowledged.

**Funding** This study was jointly sponsored by National Natural Science Foundation of China (41905067 and 42175052), the Basic Research and Operational Special Project of CAMS (2021Z007), the National Key Research and Development Program (2021YFA0718000), the Innovative Development Special Project of China Meteorological Administration (CXFZ2021Z011 and CXFZ2021Z010), and the China Meteorological Administration Forecaster Program (CMAYBY2020-166).

**Data availability** The atmospheric circulation and moisture data are from NCEP/NCAR Reanalysis data (https://psl.noaa.gov/data/gridded/data.ncep.reanalysis.pressure.html). The precipitation data are from CRA-40/Land dataset (http://www.nmic.cn/data/cdcdetail/dataCode/NAFP_CRA40_FTM_3HOR_NC.html). The NOAA OLR data are available at (https://www.esrl.noaa.gov/psd/data/gridded/data.interp_OLR.htmlhttps://www.esrl.noaa.gov/psd/data/gridded/data.interp_OLR.html). The hindcast data of BCC-CSM2-HR can be downloaded from (http://s2s.cma.cn/centers?mo=babj_CMA_37). Enquiries about post-processed data availability should be directed to the authors.

## Declarations

**Conflict of interest** The authors have not disclosed any competing interests.

## References

Adames AF, Wallace JM (2014) Three-dimensional structure and evolution of the MJO and its relation to the mean flow. J Atmos Sci 71:2007–2026. https://doi.org/10.1175/10.1175/JAS-D-13-0254.1

Andrade FM, Coelho CAS, Cavalcanti IFA (2019) Global precipitation hindcast quality assessment of the Subseasonal to Seasonal (S2S) prediction project models. Clim Dyn 52:5451–5475. https://doi.org/10.1007/s00382-018-4457-z

Brunet G, Shapiro M, Hoskins B et al (2010) Collaboration of the weather and climate communities to advance subseasonal-to-seasonal prediction. Bull Am Meteor Soc 91:1397–1406. https://doi.org/10.1175/2010BAMS3013.1

Chen WY (1982) Fluctuations in Northern Hemisphere 700 mb Height Field Associated with the Southern Oscillation. Mon Weather Rev 110(7):808–823. https://doi.org/10.1175/1520-0493(1982)110%3c0808:FINHMH%3e2.0.CO;2

Fu X, Wang B, Lee JY, Wang WQ (2011) Sensitivity of dynamical intraseasonal prediction skills to different initial conditions. Mon Weather Rev 139:2572–2592. https://doi.org/10.1175/2011MWR3584.1

Fu X, Lee JY, Hsu PC et al (2013) Multi-model MJO forecasting during DYNAMO/CINDY period. Clim Dyn 41(3–4):1067–1081. https://doi.org/10.1007/s00382-013-1859-9

Gottschalck J, Wheeler M, Weickmann K et al (2010) A framework for assessing operational Madden-Julian oscillation forecasts: a CLIVAR MJO Working Group project. Bull Am Meteor Soc 91:1247–1258. https://doi.org/10.1175/2010BAMS2816.1

Green BW, Sun S, Bleck R et al (2017) Evaluation of MJO predictive skill in Multiphysics and multimodel global ensmbles. Mon Weather Rev 145:2555–2574. https://doi.org/10.1175/MWR-D-16-0419.1

Ham YG, Schubert SD, Chang Y (2012) Optimal Initial perturbations for ensemble prediction of the Madden-Julian oscillation during boreal winter. J Clim 25:4932–4945. https://doi.org/10.1175/JCLI-D-11-00344.1

Hirons LC, Inness P, Vitart F et al (2013) Understanding advances in the simulation of intraseasonal variability in the ECMWF model. Part I: the representation of the MJO. Q J R Meteorol Soc 139:1417–1426. https://doi.org/10.1002/qj.2060

Hsu PC, Li T (2012) Role of the boundary layer moisture asymmetry in causing the eastward propagation of the Madden-Julian oscillation. J Clim 25:4914–4931. https://doi.org/10.1175/JCLI-D-11-00310.1

Hsu PC, Li T, You L, Gao J, Ren H (2015) A spatial-temporal projection method for 10–30-day forecast of heavy rainfall in Southern China. Clim Dyn 44:1227–1244. https://doi.org/10.1007/s00382-014-2215-4

Hsu PC, Lee JY, Ha KJ (2016) Influence of boreal summer intraseasonal oscillation on rainfall extremes in southern China. Int J Climatol 36:1403–1412. https://doi.org/10.1002/joc.4433

Hsu PC, Lee JY, Ha KJ, Tsou CH (2017) Influences of boreal summer intraseasonal oscillation on heat waves in Monsoon Asia. J Clim 30:7191–7211. https://doi.org/10.1175/JCLI-D-16-0505.1

Hsu PC, Qian Y, Liu Y et al (2020) Role of abnormally enhanced MJO over the Western Pacific in the formation and subseasonal predictability of the record-breaking Northeast Asian heatwave in the summer of 2018. J Clim 33:3333–3349. https://doi.org/10.1175/JCLI-D-19-0337.1

Hudson D, Marshall AG, Yin YH et al (2013) Improving intraseasonal prediction with a new ensemble generation strategy. Mon Weather Rev 141:4429–4449. https://doi.org/10.1175/MWR-D-13-00059.1

Jia X, Chen LJ, Ren FM, Li CY (2011) Impacts of the MJO on winter rainfall and circulation in China. Adv Atmos Sci 28(3):521–533. https://doi.org/10.1007/s00376-010-9118-z

Jie W, Vitart F, Wu T, Liu X (2017) Simulations of the Asian summer monsoon in the sub-seasonal to seasonal prediction project (S2S) database. Q J R Meteorol Soc 143:2282–2295. https://doi.org/10.1002/qj.3085

Kalnay E, Kanamitsu M, Kistler R et al (1996) NCEP/NCAR 40-year reanalysis project. Bull Am Meteor Soc 77(3):437–472. https://

doi.org/10.1175/1520-0477(1996)077%3C0437:TNYRP%3E2.0.CO;2
Kaufman L, Rousseeuw PJ (2009) Finding groups in data: an introduction to cluster analysis. Wiley, Hoboken
Kikuchi K, Wang B, Kajikawa Y (2012) Bimodal representation of the tropical intraseasonal oscillation. Clim Dyn 38:1989–2000. https://doi.org/10.1007/s00382-011-1159-1
Kiladis GN, Dias J, Straub KH et al (2014) A comparison of OLR and circulation-based indices for tracking the MJO. Mon Wea Rev 142(5):1697–1715. https://doi.org/10.1175/MWR-D-13-00301.1
Kim HM, Webster PJ, Toma VE et al (2014) Predictability and prediction skill of the MJO in two operational forecasting systems. J Clim 27:5364–5378. https://doi.org/10.1175/JCLI-D-13-00480.1
Kim H, Vitart F, Waliser DE (2018) Prediction of the Madden-Julian oscillation: a review. J Clim 31:9425–9443. https://doi.org/10.1175/JCLI-D-18-0210.1
Kim H, Ham YG, Joo YS et al (2021) Deep learning for bias correction of MJO prediction. Nature Commun 12:3087. https://doi.org/10.1038/s41467-021-23406-3
Lee JY, Wang B, Wheeler MC et al (2013) Real-time multivariate indices for the boreal summer intraseasonal oscillation over the Asian summer monsoon region. Clim Dyn 40:493–509. https://doi.org/10.1007/s00382-012-1544-4
Li T (2014) Recent advance in understanding the dynamics of the Madden-Julian oscillation. J Meteor Res 28(1):1–33. https://doi.org/10.1007/s13351-014-3087-6
Li W, Guo W, Qiu B et al (2018) Influence of Tibetan Plateau snow cover on East Asian atmospheric circulation at medium-range time scales. Nat Commun 9:4243. https://doi.org/10.1038/s41467-018-06762-5
Li W, Zhang Y, Shi X et al (2019) Development of the land surface model BCC_AVIM2.0 and its preliminary performance in LS3MIP/CMIP6. J Meteor Res 33:851–869. https://doi.org/10.1007/s13351-019-9016-y
Li T, Ling J, Hsu PC (2020) MaddenJulian oscillation: its discovery, dynamics, and impact on East Asia. J Meteor Res 34(1):20–42. https://doi.org/10.1007/s13351-020-9153-3
Liang X, Jiang LP, Pan Y et al (2020) A 10-yr global land surface reanalysis interim dataset (CRA-Interim/Land): Implementation and preliminary evaluation. J Meteor Res 34(1):101–116. https://doi.org/10.1007/s13351-020-9083-0
Liebmann B, Smith CA (1996) Description of a complete (interpolated) outgoing longwave radiation dataset. Bull Am Meteor Soc 77:1275–1277. https://doi.org/10.1175/1520-0477-77.6.1274
Lim Y, Son S, Kim D (2018) MJO prediction skill of the subseasonal-to-seasonal prediction models. J Clim 31:4075–4094. https://doi.org/10.1175/JCLI-D-17-0545.1
Liu X, Wu T, Yang S et al (2017) MJO prediction using the sub-seasonal to seasonal forecast model of Beijing Climate Center. Clim Dyn 48(9–10):3283–3307. https://doi.org/10.1007/s00382-016-3264-7
Liu X, Li W, Wu T et al (2019) Validity of parameter optimization in improving MJO simulation and prediction using the sub-seasonal to seasonal forecast model of Beijing Climate Center. Clim Dyn 52:3823–3843. https://doi.org/10.1007/s00382-018-4369-y
Liu B, Yan Y, Zhu C et al (2020) Record-breaking Meiyu rainfall around the Yangtze River in 2020 regulated by the subseasonal phase transition of the North Atlantic oscillation. Geophys Res Lett 47:e2020GL090342. https://doi.org/10.1029/2020GL090342
Liu X, Yao J, Wu T et al (2021a) Development of coupled data assimilation with the BCC climate system model: highlighting the role of sea-ice assimilation for global analysis. Journal of Advances in Modeling Earth Systems 13:e2020MS002368. https://doi.org/10.1029/2020MS002368
Liu Y, Fan K, Chen L et al (2021b) An operational statistical downscaling prediction model of the winter monthly temperature over China based on a multi-model ensemble. Atmos Res 249:105262. https://doi.org/10.1016/j.atmosres.2020.105262
Liu Y, Hu ZZ, Wu R et al (2021c) Subseasonal prediction and predictability of summer rainfall over eastern China in BCC_AGCM2.2. Clim Dyn 56:2057–2069. https://doi.org/10.1007/s00382-020-05574-y
Madden RA, Julian PR (1971) Detection of a 40–50 day oscillation in the zonal wind in the tropical Pacific. J Atmos Sci 28(5):702–708.
Madden RA, Julian PR (1972) Description of global-scale circulation cells in the tropics with a 40–50 day period. J Atmos Sci 29(6):1109–1123. https://doi.org/10.1175/1520-0469(1972)029%3C1109:dogscc%3E2.0.co;2
Raghunathan TE, Rosenthal R, Rubin DB (1996) Comparing correlated but nonoverlapping correlations. Psychol Methods 1(2):178–183. https://doi.org/10.1037/1082-989X.1.2.178
Ren HL, Ren P (2017) Impact of Madden-Julian Oscillation upon winter extreme rainfall in Southern China: Observations and predictability in CFSv2. Atmosphere 8(12):192. https://doi.org/10.3390/atmos8100192
Ren P, Ren HL, Fu JX et al (2018) Impact of boreal summer intraseasonal oscillation on rainfall extremes in southeastern China and its predictability in CFSv2. J Geophys Res Atmos 123:4423–4442. https://doi.org/10.1029/2017JD028043
Schwartz C, Garfinkel CI (2020) Troposphere-stratosphere coupling in subseasonal-to-seasonal models and its importance for a realistic extratropical response to the Madden-Julian oscillation. J Geophys Res Atmos 125:e2019JD032043. https://doi.org/10.1029/2019JD03204310.1029/2019JD032043
Shibuya R, Nakano M, Kodama C et al (2021) Prediction skill of the boreal summer intra-seasonal oscillation in global non-hydrostatic atmospheric model simulations with explicit cloud microphysics. J Meteorol Soc Jpn 99(4):973–992. https://doi.org/10.2151/jmsj.2021-046
Stan C, Straus DM, Frederiksen JS et al (2017) Review of tropical-extratropical telconnections on intraseasonal time scale. Rev Geophys 55(4):902–937. https://doi.org/10.1002/2016RG000538
Taraphdar S, Zhang F, Leung LR, Chen X, Pauluis OM (2018a) MJO affects the monsoon onset timing over the Indian region. Geophys Res Lett 45:10011–10018. https://doi.org/10.1029/2018aGL078804
Taraphdar S, Zhang F, Leung LR, Chen X, Pauluis OM (2018b) MJO affects the monsoon onset timing over the Indian region. Geophys Res Lett 32(45):10011–10018. https://doi.org/10.1029/2018GL078804
Vitart F (2014) Evolution of ECMWF sub-seasonal forecast skill scores. Q J R Meteorol Soc 140:1889–1899. https://doi.org/10.1002/qj.2256
Vitart F, Ardilouze C, Bonet A et al (2017) The subseasonal to seasonal (S2S) prediction project database. Bull Am Meteor Soc 98:163–175. https://doi.org/10.1175/BAMS-D-16-0017.1
Wang S, Ma D, Soble AH et al (2018) Propagation characteristics of BSISO indices. Geophys Res Lett 45:9934–9943. https://doi.org/10.1029/2018GL078321
Wang S, Sobel AH, Tippett MK et al (2019) Prediction and predictability of tropical intraseasonal convection: seasonal dependence and the Maritime Continent prediction barrier. Clim Dyn 52:6015–6031. https://doi.org/10.1007/s00382-018-4492-9
Wheeler MC, Hendon HH (2004) An all-season real-time multivariate MJO index: development of an index for monitoring and prediction. Mon Weather Rev 132:1917–1932. https://doi.org/10.1175/1520-0493(2004)132%3C1917:Aarmmi%3E2.0.Co;2
Wu J, Gao XJ (2013) A gridded daily observation dataset over China region and comparison with the other datasets. Chin J Geophys

56(4):1102–1111. https://doi.org/10.6038/cjg20130406 (**in Chinese**)

Wu J, Jin FF (2021) Improving the MJO forecast of S2S operation models by correcting their biases in linear dynamics. Geophys Res Lett 48(6):e2020GL091930. https://doi.org/10.1029/2020GL091930

Wu J, Ren HL, Zuo J et al (2016) MJO prediction skill, predictability, and teleconnection impacts in the Beijing climate center atmospheric general circulation model. Dyn Atmos Oceans 75:78–90. https://doi.org/10.1016/j.dynatmoce.2016.06.001

Wu T, Lu Y, Fang Y et al (2019) The Beijing Climate Center Climate System Model (BCC-CSM): the main progress from CMIP5 to CMIP6. Geosci Model Dev 12:1573–1600. https://doi.org/10.5194/gmd-12-1573-2019

Wu J, Ren HL, Lu B et al (2020) Effects of moisture initialization on MJO and its teleconnection prediction in BCC subseasonal coupled model. J Geophys Res Atmos 125(1):e2019JD031537. https://doi.org/10.1029/2019JD031537

Wu T, Yu R, Liu Y et al (2021) BCC-CSM2-HR: a high-resolution version of the Beijing Climate Center Climate System Model. Geosci Model Dev 14:2977–3006. https://doi.org/10.5194/gmd-14-2977-2021

Xie PP, Arkin PA (1997) Global precipitation: A 17-year monthly analysis based on gauge observations, satellite estimates, and numerical model outputs. Bull Amer Meteor Soc 78:2539–2558

Xie PP, Yatagai A, Chen M et al (2007) A gauge-based analysis of daily precipitation over East Asia. J Hydrometeorol 8:607–626

Yang QM, Li Y, Song J, Huang SC (2012) Study on the extended range forecast of the principal 20–30-day oscillation pattern of the circulation over East Asia in summer of 2002. Acta Meteorol Sin 26:554–565. https://doi.org/10.1007/s13351-012-0502-8

Zhang CD (2005) Madden-Julian oscillation. Rev Geophys 43:RG2003. https://doi.org/10.1029/2004RG000158

Zhang C (2013) Madden-Julian Oscillation—bridging weather and climate. Bull Am Meteor Soc 91(94):1849–1870. https://doi.org/10.1175/BAMS-D-12-00026.1

Zhang C, Zhang B (2018) QBO-MJO connection. J Geophys Res Atmos 123:2957–2967. https://doi.org/10.1002/2017JD028171

Zhao C, Ren HL, Eade R et al (2019) MJO modulation and its predictability of boreal summer tropical cyclone genesis over northwest Pacific in Met Office Hadley Centre and Beijing Climate Center seasonal prediction systems. Q J R Meteorol Soc 145(720):1089–1101. https://doi.org/10.1002/qj.3478

Zheng L, Zhang Y, Huang A (2020) Sub-seasonal prediction of the 2008 extreme snowstorms over South China. Clim Dyn 55:1979–1994. https://doi.org/10.1007/s00382-020-05361-9

Zhu Z, Li T (2017) The statistical extended range (10–30 day) forecast of summer rainfall anomalies over the entire China. Clim Dyn 48(1):209–224. https://doi.org/10.1007/s00382-016-3070-2

Zhu Z, Li T (2018) Extended-range forecasting of Chinese summer surface air temperature and heat waves. Clim Dyn 50:2007–2021. https://doi.org/10.1007/s00382-017-3733-7

Zhu Z, Li T, Hsu PC, He J (2015) A spatial-temporal projection for extended-range forecast in the tropics. Clim Dyn 45:1085–1098. https://doi.org/10.1007/s00382-014-2353-8

Zhu Y, Zhou X, Li W et al (2018) Toward the improvement of subseasonal prediction in the National Centers for Environmental Prediction Global Ensemble Forecast System. J Geophys Res Atmos 123:6732–6745. https://doi.org/10.1029/2018JD028506

Zhu X, Liu X, Huang A et al (2021) Impact of the observed SST frequency in the model initialization on the BSISO prediction. Clim Dyn 57:1097–1117. https://doi.org/10.1007/s00382-021-05761-5